

Interpretable statistical representations of neural population dynamics and geometry

Adam Gosztolai^{1,*}, Robert L. Peach^{2,3}, Alexis Arnaudon^{4,†}, Mauricio Barahona⁴, and Pierre Vandergheynst¹

¹Signal Processing Laboratory (LTS2), EPFL, Lausanne, Switzerland

²Department of Brain Sciences, Imperial College London, London, United Kingdom

³Department of Neurology, University Hospital Würzburg, Würzburg, Germany

⁴Department of Mathematics, Imperial College London, London, United Kingdom

Abstract

The dynamics of neuron populations during diverse tasks often evolve on low-dimensional manifolds. However, it remains challenging to discern the contributions of geometry and dynamics for encoding relevant behavioural variables. Here, we introduce an unsupervised geometric deep learning framework for representing non-linear dynamical systems based on statistical distributions of local phase portrait features. Our method provides robust geometry-aware or geometry-agnostic representations for the unbiased comparison of dynamics based on measured trajectories. We demonstrate that our statistical representation can generalise across neural network instances to discriminate computational mechanisms, obtain interpretable embeddings of neural dynamics in a primate reaching task with geometric correspondence to hand kinematics, and develop a decoding algorithm with state-of-the-art accuracy. Our results highlight the importance of using the intrinsic manifold structure over temporal information to develop better decoding algorithms and assimilate data across experiments.

Introduction

Understanding how neural dynamics collectively encode behaviourally relevant computations is a fundamental challenge in neuroscience. An increasing number of works have focused on the geometry of neural manifolds – low-dimensional smooth subspaces to which the high-dimensional neural activities are constrained – as the object that defines task-relevant computations [1]–[6]. In contrast, others have suggested that computations comprise the dynamical flows of neural population activity over manifolds [7], [8] and that manifold geometry is merely an imprint of these dynamics which may change across animals or over time within the same animal [9]. Recent high-fidelity measurements of large-scale neural activity [10]–[12] and behaviour [13]–[15] provide experimental access to address this dichotomy in different contexts. However, the utility of either viewpoint hinges on theoretical frameworks and computational methods that address the challenges associated with finding unbiased representations that are comparable across experiments, interpretable based on behavioural variables, and can decouple the contributions of geometry and dynamics.

Current approaches for learning representations of dynamical measurements do not meet the above challenges. Dynamical models provide accurate predictions of given time series observables [16]–[20], yet they implicitly depend on the manifold geometry and thus require additional transformations to align latent representations across measurements [19], [20]. Manifold learning approaches can effectively unfold the underlying manifold structure but treat phase portraits as point clouds [21], [22] and thus cannot decouple dynamics and manifold geometry. Likewise, topological data analysis methods find topological invariants in the data [2], [4], [23] while disregarding the dynamics and

*corresponding author: adam.gosztolai@epfl.ch

†Current address: Blue Brain Project, École polytechnique fédérale de Lausanne (EPFL), Campus Biotech, Geneva, Switzerland

manifold geometry. Instead, we seek a framework that can *intrinsically* represent the dynamics over the manifold, which would ensure transferability across datasets, and can flexibly account for the geometry of the manifold.

Here we introduce a theoretical framework and computational method by combining ideas from empirical dynamical modelling [24], [25] and the statistical descriptions of interacting dynamical systems [26], [27] to learn intrinsic representations of non-linear dynamics over manifolds. Specifically, instead of learning the dynamics globally, as achieved by current dynamical models and geometric deep learning methods [28]–[33], we focus on local vector field features of the dynamical phase portrait. This viewpoint relies on the intuitive idea that local features are preserved, in intrinsic coordinates, under continuous deformations or reorientations of the manifold. To leverage this idea, we present a fully unsupervised method, called MARBLE, that combines geometric deep learning [34]–[36] and contrastive learning [37] to learn a similarity-preserving embedding from vector field features to points in a shared latent space giving a statistical representation of the dynamical system. By toggling the rotation invariance of local vector field embeddings, our representations can encode both dynamics and the manifold geometry, or only the dynamics irrespective of the manifold geometry, to test scientific hypotheses. We demonstrate that our framework allows the unbiased comparison of deterministic non-linear dynamical systems for inferring global system transitions and robustly discriminating computational solutions obtained by recurrent neural networks (RNNs) trained on neuroscience tasks. We interpret these local representations in terms of macroscopic system properties, such as system states, decision variables and behavioural kinematics. Further, in electrophysiological recordings in macaques during a reaching task, we discover a geometric correspondence between the statistical representations of the neural dynamics and physical space configurations. We use these representations to decode kinematic trajectories, obtaining significantly above state-of-the-art accuracy.

Results

Data-driven distributional representation of vector fields over manifolds

To characterise the neural computations underpinning behaviour, e.g., decision-making or motor actions, a typical neuroscience task involves a set of trials resulting in d -dimensional time-series measurements $\{\mathbf{x}(t)\}$ of the state of an animal, e.g., neural activity or behavioural kinematics. Frequently, these experiments are replicated under diverse experimental conditions, requiring an unbiased comparison between sets of trajectories to reveal alterations in neural mechanisms. This is often challenging for two reasons. First, differently initialised trajectories across trials produce uneven and sparse sampling of the relevant basins of attraction of the dynamics. Second, similar dynamics may be embedded in different manifolds across subjects, making a direct global comparison difficult.

To address these challenges, instead of learning the temporal evolution of the states, we build a statistical representation of the dynamics based on the spatial context of sample points. This is possible because the trajectories of neural dynamics [7] or more generally of dissipative dynamical systems [38] converge to an m -dimensional manifold \mathcal{M} embedded into the larger original d -dimensional state-space (Fig. 1a). As a first step, we treat the trajectories under an experimental condition c as a vector field $\mathbf{F}_c = (\mathbf{f}_1, \dots, \mathbf{f}_n)$ anchored at a point cloud $\mathbf{X}_c = (\mathbf{x}_1, \dots, \mathbf{x}_n)$ (Fig. 1b). To approximate the geometry of the underlying manifold, we fit a proximity graph to \mathbf{X}_c . The local context of a point i is then described by the vector field in the p -hop neighbourhood of i . Second, we embed these individual local features into a shared latent space to obtain latent vectors $\mathbf{Z}_c = (\mathbf{z}_1, \dots, \mathbf{z}_n)$. These allow us to represent the dynamical system as an empirical distribution $P_c = \sum_i^n \delta(\mathbf{z}_i)$, where δ is the Dirac delta function. Being defined in the same space, these distributions can be compared to create a measure of distance between dynamical systems. For this, we use the optimal transport distance (Eq. (18)) between these distributions that relies on the similarity in the feature space to relate datasets.

The above approach requires a mapping from vector field features to latent vectors that are similarity-preserving and can detect overlaps between the feature distributions of dynamical systems embedded over distinct manifolds. To learn such a mapping, we develop an unsupervised geometric deep learning method, called MARBLE, whose core architecture consists of four components (Fig. 1c); an optional vector diffusion kernel with learnable parameter τ (Eq. (3)), which tunes the resolution of the features; p gradient filter layers (Eq. (13)), whose output together with \mathbf{f}_i gives the best p -th order approximation of the local vector field around i ; inner product features involving with

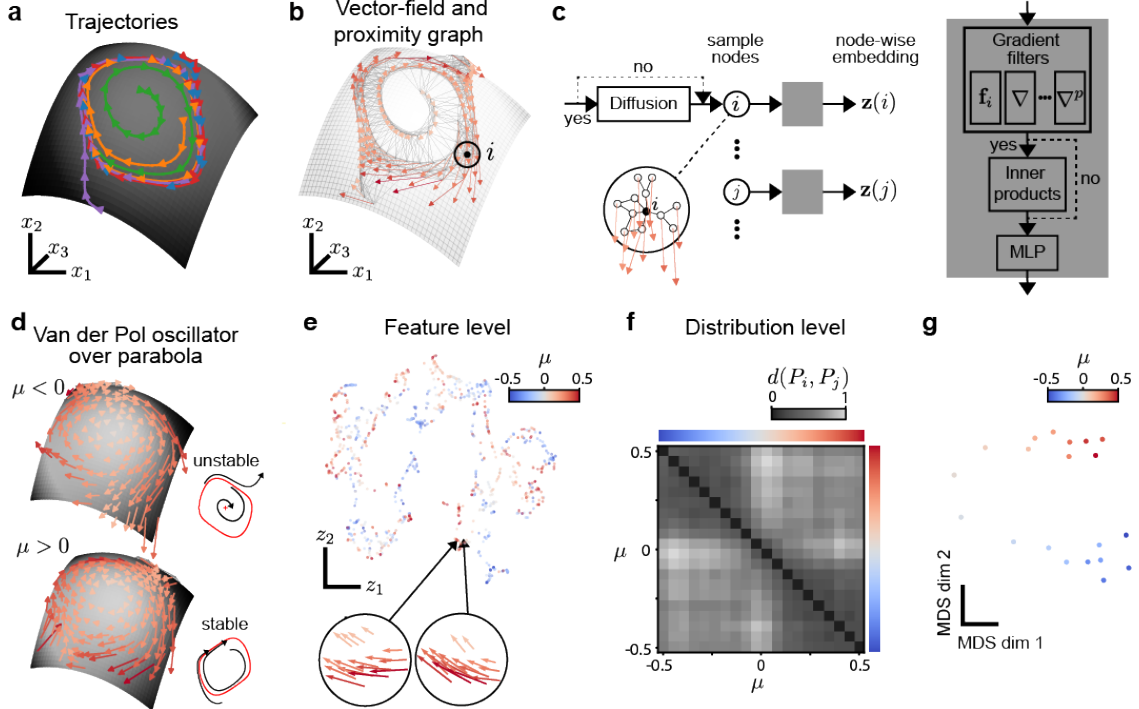


Figure 1: Statistical representation of time-series measurements of dynamics evolving over manifolds. **a** State-space representation of four trajectories obtained in different trials indicated by the colours. Lines and arrows guide the eye. The parabolic manifold is shown for illustration. **b** Vector field representation of dynamics based on the sampled points. The samples are connected by a k -nearest neighbour graph to approximate the shape of the manifold. One sample and the corresponding local vector field feature are denoted by the black circle. **c** Geometric deep learning model for the node-wise embedding of local features. The vector field is first smoothed by an optional vector diffusion layer. The local features of nodes are approximated by gradient filters up to p -th order and optionally transformed into rotation-invariant inner product features. Finally, a multilayer perceptron (MLP) embeds features into a common latent space where close points correspond to similar features as shown in insets. **d** Phase portraits of the Van der Pol oscillator embedded over a parabolic manifold at two parameter regimes containing an unstable $\mu = -0.25$ and stable limit $\mu = 0.25$ cycle respectively, see insets showing a vertical projected view. The vector fields were sampled from randomly initialised trajectories ($n \approx 200$). **e** Latent space embedding of local features of state spaces under 20 different conditions visualised in two dimensions via UMAP embedding. **f** Matrix of distribution distances across conditions. The clusters indicate an abrupt dynamical change at $\mu = 0$, corresponding to the Hopf bifurcation. **g** Two-dimensional MDS embedding of the distance matrix showing that the ordering of parameter μ is also recovered over two weakly connected one-dimensional manifolds.

learnable linear transformations (Eq. (15)), which make the gradient features rotation invariant; and a multilayer perceptron (MLP) with learnable weights ω that produce the latent vectors \mathbf{z}_i . Unsupervised training of the network is possible due to the continuity of dynamical features over the manifold, allowing the features of adjacent nodes to be embedded close in latent space while embedding those of randomly sampled nodes further apart. By imposing this as a soft constraint in the loss function of the optimisation (Eq. (17)), we can identify similar features across different parts of the same manifold and manifolds.

The optional components of the MARBLE network give rise to two operation modes designed to decouple the dynamics from the manifold geometry. In geometry-aware mode, the inner product features are disabled to obtain maximally expressive embeddings that contain information about both the geometry of the manifold and the dynamics evolving over the manifold. Alternatively, in geometry-agnostic mode, inner product features ensure that the network only learns information about the vector field variation within neighbourhoods and not their spatial orientation (Figs. 7–8) at a slight cost of expressivity. This mode should be used whenever the manifold geometry and orientation are expected to play no role in the computation. In addition, the optional vector diffusion layer smoothens the vector field, making our method more broadly applicable to noisy dynamical systems whose dynamics evolve near but not exactly on a manifold.

Local features detect continuous and abrupt changes in global dynamics

Varying the underlying parameter of a dynamical system can cause both continuous changes such as slowing down or speeding up, or abrupt, qualitative transitions, such as bifurcations. As an illustrative example, we use the well-known Van der Pol oscillator that is unstable for negative damping parameter μ and stabilises as μ increases above zero in a Hopf bifurcation (Fig. 1d and Eq. (19)). In addition, increasing $|\mu|$ causes continuous deformations of the limit cycle from circular to asymmetric corresponding to slow-fast dynamics. To showcase our method on a non-trivial manifold, we additionally map the Van der Pol system to a parabola.

To identify the transition at $\mu = 0$, we simulated short trajectories from random initial conditions for 20 different values of μ and obtained vector fields for each. Then, we trained a geometry-agnostic MARBLE network to embed the local features into a common five-dimensional latent space. We visualise it in two dimensions via the UMAP projection algorithm [39] (Fig. 1e). The embedded points show overlap even across conditions, reflecting the ability of the method to embed similar features across manifolds correctly. For larger $|\mu|$, the points become more disjoint, as most local features show either strong convergent or divergent trajectories.

Despite the proximity of individual features in the latent space, at the distributional level, the embeddings can globally discriminate the dynamical systems across μ . Indeed, computing the optimal transport distance $d(P_i, P_j)$ (Eq. (18)) between pairs of empirical distributions associated with conditions μ_i, μ_j yields a matrix with a two-partition structure for positive and negative μ (Fig. 1f). For the geometric-agnostic network, this structure was stable under manifold deformations introduced by randomly changing the curvature of the parabola, but was lost when we trained a geometry-aware network (Fig. 9). In addition, this distance matrix also encodes continuous deformation of the dynamical system, which can be revealed by linearly embedding the distance matrix with the multidimensional scaling (MDS) algorithm (Fig. 1g) into 2D space. This embedding shows that the points corresponding to conditions distribute over a 1D manifold with noise, on which the ordering of the μ is preserved. This order is unexpected since it emerges from the distributional changes of irregularly spaced features over the manifold. Taken together, MARBLE can thus distinguish abrupt (stable/unstable) and continuous (change of $|\mu|$) deformation of dynamical systems on manifolds from a collection of short trajectories.

Discriminating computational mechanisms in recurrent neural networks

Recent years have seen significant interest in using RNNs as a surrogate for the computations performed by the brain during diverse tasks [7], [40]–[42]. Previous approaches for comparing the computational solutions obtained by RNNs in a given task relied on static representations based on snapshots of population activity [40], [43], [44]. However, these methods cannot distinguish dynamical processes that produce similar static representations and require distributional alignment of these representations to account for possibly different embeddings of the dynamics.

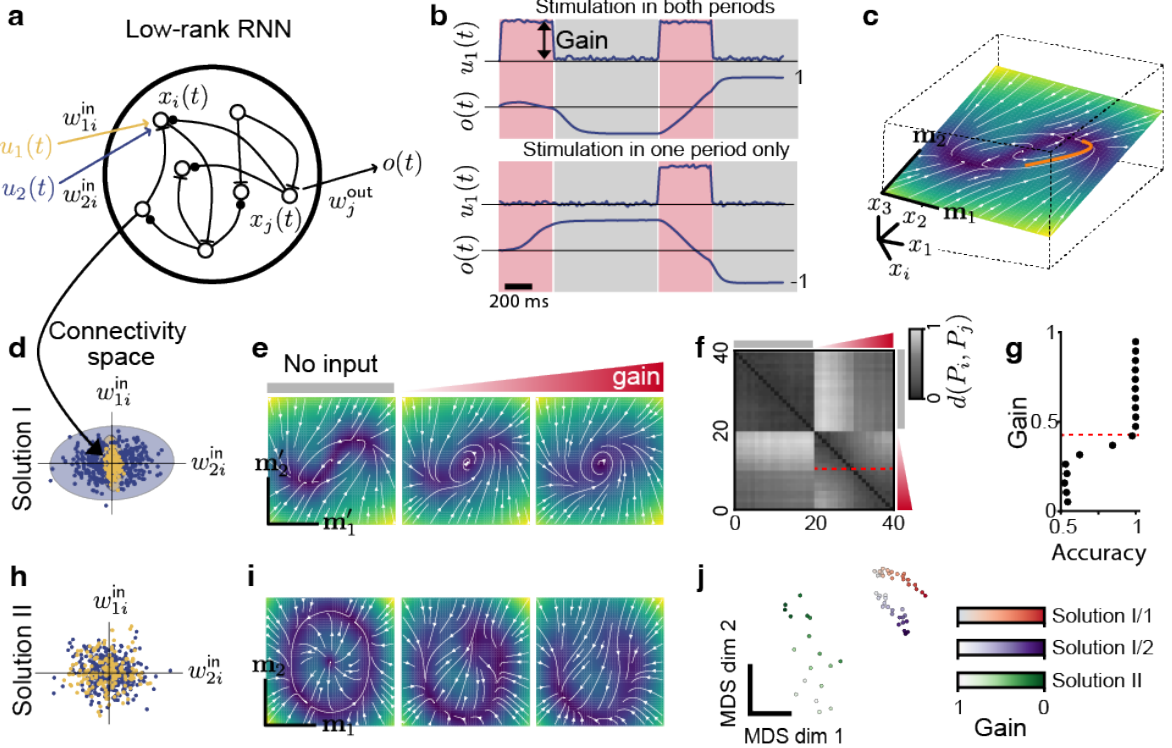


Figure 2: Distributional representations discriminate computations across instances of recurrent neural networks. **a** Low-rank RNN, taking as input two stimuli and producing a decision variable as the output. Flat and circular arrow endings represent inhibitory and excitatory connections. **b** Two example input patterns for one of the stimuli lead to two different decision outcomes. The amplitude of the inputs is controlled by the gain. Red and grey-shaded bands show stimulated and unstimulated epochs. **c** Illustration of the low dimensional internal dynamics of a trained low-rank RNN in high-dimensional state-space. The vector field shows mean field dynamics superimposed with a sample trajectory (orange). **d** Distribution of input weights for all nodes i in one network solution. The neurons form two clusters, each specialising in one input. Ellipses represent 3 std bands of a fitted Gaussian distribution to the clustered coefficients. **e** Phase portraits of the mean-field dynamics for no input and gradually increasing the input gain. **f** Matrix of distances between embedded feature distributions between experiments at different input gains. The red dashed line marks two clusters obtained with hierarchical clustering corresponding to a bifurcation in the dynamics as the gain is varied. **g** Accuracy against input gain, red dashed line marks the prediction obtained from **f**. **h** Same as **d**, but for another network solution. Here, network nodes show no clustering, implying that the neurons generalise to process both stimuli. **i** Same as **e**, but for the network solution in **h**. **j** MDS embedding of the distance matrix corresponding to the embedding of the gain-modulated dynamics. The embeddings of two samples of network solution I fall closer than those of network solution II. Dots correspond to a condition at the given gain.

To address these shortcomings, we replicated the delayed-match-to-sample (DMS) task of [45] by training RNNs with a rank-two connectivity matrix (see Materials and Methods, Section 3.1), which were previously shown to be sufficiently expressive [46]. The task is commonly used in contextual decision-making and comprises two distinct stimuli with variable gain as well as two stimulation epochs of variable duration interspersed by a delay (Fig. 2b). After setting the gain to unity, the RNN network was trained to converge to an output of 1 if either stimulus was presented during both epochs and -1 otherwise (Fig. 2b). As expected [47], following training the internal dynamics of the network settled on a plane oriented randomly in neural state-space (Fig. 2c and Fig. 10). In addition, we found that the optimisation of differently initialised networks converges to two classes of solutions as shown by the different distributions of the input weights $\mathbf{w}_1^{\text{in}}, \mathbf{w}_2^{\text{in}}$ (Fig. 2d,h, Eq. (22)): solution I consist of two subpopulations specialised in sensing the two stimuli, whilst in solution II the nodes generalise across the two stimuli. These solutions exhibit substantially different internal dynamics as shown by two representative examples, which we selected for further analysis (Fig. 2e,i).

Since the task requires detecting the presence of two stimuli, we hypothesised that progressively smaller gains will lead to either an abrupt or gradual loss in task performance. To test whether MARBLE can capture these changes based on the network dynamics, we recorded trajectories for solution I in 200 randomly initialised trials for 20 different input gains (Fig. 10) and performed a PCA embedding into three dimensions which explained over 99% of the variance. Since the internal dynamics are shaped by the inputs, we expected the phase portrait to be the same at a given stimulation gain. Thus, we split the trajectories between epochs forming 20 groups of sub-trajectories at no input and 20 groups at different gains. We then trained a geometry-aware MARBLE network to jointly embed these 40 groups over distinct manifolds into common latent space. The matrix of pairwise distribution distances displays a block-diagonal structure (Fig. 2f). The top left block corresponds to unstimulated conditions whose close-to-zero entries imply highly overlapping features across phase portraits, showing that our method obtains similar representations despite stark differences in sampling. Meanwhile, the bottom right block has two further sub-blocks, corresponding to an abrupt change in the phase portrait, which remarkably corresponds to a sudden drop of accuracy (Fig. 2g) from 1 to 0.5 (random). This indicates that MARBLE can detect information in the dynamics of such RNN networks in an unsupervised manner that is relevant for global decision variables.

We then asked whether, in addition to detecting dynamical changes within the same RNN solution, our method can also meaningfully compare dynamical changes across RNN instances. To test this, we used the fact that low-rank RNNs sampled from the same Gaussian weight distribution have the same mean field dynamics [46] albeit on differently oriented manifolds. Thus, we generated two new networks from solution I by randomly sampling their weights from Gaussian distributions fitted to weights of the original network (Fig. 2d), serving as a negative control, and compared their dynamics to solution II. As before, we simulated 200 trials of these three RNNs and produced feature embeddings of their dynamics during stimulation with the geometry-agnostic MARBLE network. The MDS embedding of the distance matrix (Fig. 2j) shows that MARBLE can cluster each of the three RNN solutions separately while retaining the underlying continuous change of gain. Further, our model embeds two variants of solution I closer to each other than to solution II. These findings confirm that our method can be used to reliably compare dynamical processes generated by different system architectures with possible implications towards guiding their design for faster training, and more robust and accurate predictions.

Representing and decoding neural dynamics in a macaque reaching task

Finally, to show that our distributional representations can be used to interpret neural dynamics in terms of behavioural variables, we reanalysed the electrophysiological recordings from [19] of a macaque performing a delayed centre-out arm-reaching task. During the task, a trained monkey was instructed to move a handle towards seven distinct targets placed at radial locations from the start position. The dataset involved simultaneous kinematic tracking of the hand (Fig. 3a) and neural activity recorded via a 24-channel probe inserted into the premotor cortex (PMd) over 44 recording sessions (Fig. 3b shows one session).

Since a subset of neurons in the premotor cortex is directionally tuned [48], we argued that the representation of the neural dynamics must account for the orientation of the neural manifold. Thus, we trained a geometry-aware MARBLE network on each session to produce feature embeddings of the firing rate traces as follows (Fig. 3c). Further, to test if behaviourally interpretable embeddings emerge

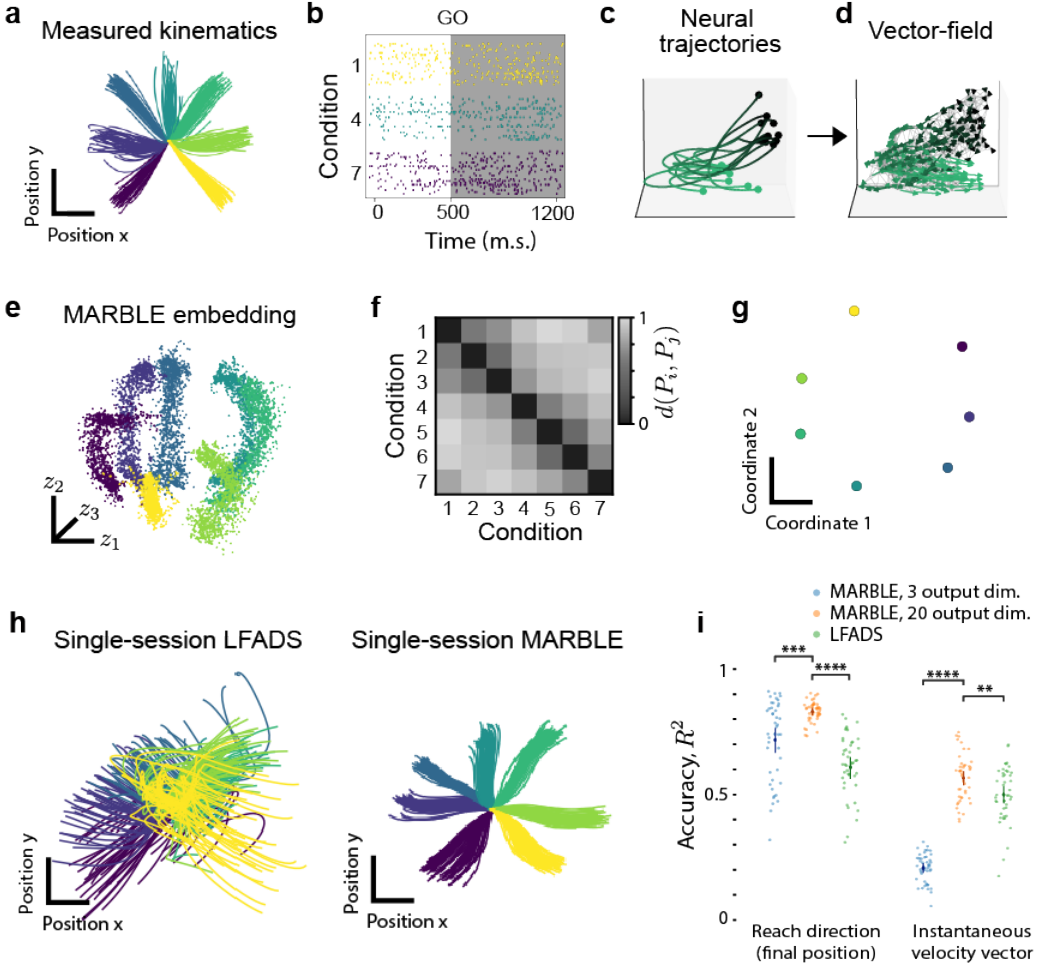


Figure 3: Distributional representation of neural activity in premotor cortex has geometric correspondence to behavioural kinematics in a macaque centre-out reaching task. **a** Ground truth hand trajectories in seven reaching directions. **b** Exemplary single-trial spike-trains from a single recording session for each of the respective reaching directions. Rows within a given colour (condition) correspond to 24 recording channels. The shaded area corresponds to the analysed traces after the GO cue. **c** Ten representative neural firing rate trajectories PCA-embedded from 24 to three dimensions for visualisation. Shading from black to the respective colours represents the arrow of time. **d** Ensembles of trajectories are used to construct vector fields over distinct manifolds for each condition and described by a proximity graph. Data from all conditions in a single session are used to train a MARBLE network. **e** Feature embeddings obtained from MARBLE in a given session. The 3D-embedded points reflect the arrangement of reaches in physical space. **f** Matrix of distribution distances between pairwise conditions averaged across sessions showing periodic structure. **g** MDS embedding of the distance matrix recovers the spatial arrangement of reaches. **h** Hand trajectories linearly decoded from a representative session for a state-of-the-art LFADS model and from the MARBLE embeddings. **i** Decoding accuracy as measured by the variance explained (R^2) between the ground truth and decoded sessions across the entire dataset for the final position (left) and instantaneous velocity (right). Wilcoxon tests (paired samples), **: $p < 1 \times 10^{-2}$, ***: $p < 1 \times 10^{-3}$, ****: $p < 1 \times 10^{-4}$.

from the neural dynamics without imposing geometric relationships across conditions, we constructed separate vector fields for each reaching condition (Fig. 3d) and fed points randomly from each of the seven conditions during training into a single MARBLE network. We found that, unlike the popular latent factor encoding of neural dynamics 11, the local feature embeddings in 3D strongly reflect the spatial orientation of the physical reaches (Fig. 3e and Fig. 11). This geometric configuration is also confirmed by the diagonal and periodic structure of the condition-averaged distance matrix between feature distributions across reach directions (Fig. 3f) and its associated MDS embedding (Fig. 3g). Our findings thus show that the geometry and dynamics of the neural code strongly encode reach configurations in physical space.

The ability of our method to unfold the global geometry and dynamics suggests a novel decoding algorithm. Current decoders use temporal information [19], [20], but here we asked whether better decoding performance can be achieved by using the additional structure offered by the manifold context. To compare to previous works, we fitted an optimal linear estimator between the feature embeddings of each timepoint and the corresponding hand position. Remarkably, the decoded kinematics using MARBLE outperformed the state-of-the-art LFADS model [19] in both accuracy and consistency (Fig. 3h). This is quantified by the significantly higher accuracy in the reach direction (Fig. 3i) for all output dimensions. However, we find that the dimension of the MARBLE embedding space must be increased to accurately represent the delay between the GO cue and the beginning of the movement (Fig. 3i). These results highlight that MARBLE can generate representations of neural dynamics that are simultaneously interpretable and decodable into behavioural variables.

Discussion

Generating insights into how the brain and other collective systems perform population-level computations requires both large-scale temporally resolved measurements [49] and computational methods for representing the measured dynamics. Specifically, these representations must enable unbiased comparisons across different instances of the systems, be interpretable in terms of global variables, such as behavioural states, and be useful for downstream tasks like decoding and prediction. The growing recognition of the prevalence and importance of manifold-constrained dynamics [1]–[4] poses a need for methods that use manifold geometry as an inductive bias.

To address this need, we have developed the MARBLE framework for representing dynamical systems based on the distribution of local vector field features over the dynamical manifold. Our results show that the local features collectively encode global information about the macroscopic properties of the collective system, such as dynamical states or behavioural variables. Further, by making local features rotation invariant one can obtain representations that are robust to embedding a given dynamics over different manifolds. Importantly, this enables the hypothesis-driven use of MARBLE in geometry-aware or geometry-agnostic mode, depending on whether or not the manifold geometry is relevant to the particular application. In this sense, our approach diverges from geometric deep learning models that learn vector fields globally without decomposing into local features, such as Refs. [31], [33], [36] which therefore cannot flexibly decouple the manifold geometry from the dynamics. Further, since our representation is intrinsic, i.e., it depends only on the local manifold structures, local representations allow assimilating different datasets without fitting additional parameters to build more powerful MARBLE models.

Although there are many ways to represent a dynamical system depending on the application, we provide here a general, model-free approach to be used as a first-line tool for studying the dynamical effect of experimental interventions before constructing more specific model-based methods. Further, the unique ability of our approach to learning global properties of dynamics from local features points towards building predictive models that rely on manifold context in addition to temporal information, for example, using modern transformer architectures. Manifold consistency also poses a strong regularity assumption over the possible dynamics which opens up new avenues for designing scientific hypotheses and validating experimental findings. In summary, our distributional approach provides a powerful tool for studying dynamical systems with applications in theoretical and experimental research.

Code availability

The code to carry out the simulations and analysis can be found at github.com/agosztolai/MARBLE.

Data availability

The data generated during the simulations is available with DOI: [10.7910/DVN/KTE4PC](https://doi.org/10.7910/DVN/KTE4PC).

Acknowledgements

We thank Nicolas Aspert for the much-needed computing support. We also thank Adrian Valente, Nikolas Karalias and Matteo Vinao-Carl for the interesting discussions.

AG acknowledges support from an HFSP Cross-disciplinary Postdoctoral Fellowship (LT000669/2020-C). MB acknowledges funding through EPSRC awards EP/N014529/1 (Centre for Mathematics of Precision Healthcare) and EP/W024020/1 (Statistical Physics of Cognition). RP acknowledges the Deutsche Forschungsgemeinschaft (DFG, German Research Foundation) Project-ID 424778381-TRR 295.

Author contributions

Conceptualisation: A.G., R.L.P., A.A., M.B., P.V., Methodology: A.G., R.L.P., A.A., P.V., Software: A.G., R.L.P., A.A., Analysis: A.G., R.L.P., A.A., Writing - Original Draft: A.G., R.L.P., A.A., Writing - Review & Editing: M.B., P.V.

Competing interests

The authors declare no competing interests.

References

- [1] S. Chung, D. D. Lee, and H. Sompolinsky, “Classification and geometry of general perceptual manifolds,” *Phys. Rev. X*, vol. 8, no. 3, p. 31003, 2018.
- [2] R. Chaudhuri, B. Gervek, B. Pandey, *et al.*, “The intrinsic attractor manifold and population dynamics of a canonical cognitive circuit across waking and sleep,” *Nat. Neurosci.*, vol. 22, no. 9, pp. 1512–1520, 2019.
- [3] M. Khona and I. R. Fiete, “Attractor and integrator networks in the brain,” *Nat. Rev. Neurosci.*, vol. 23, no. 12, pp. 744–766, 2022.
- [4] R. J. Gardner, E. Hermansen, M. Pachitariu, *et al.*, “Toroidal topology of population activity in grid cells,” *Nature*, vol. 602, no. 7895, pp. 123–128, 2022.
- [5] R. Nogueira, C. C. Rodgers, R. M. Bruno, *et al.*, “The geometry of cortical representations of touch in rodents,” *Nat. Neurosci.*, vol. 26, no. 2, pp. 239–250, 2023.
- [6] M. Beiran, N. Meirhaeghe, H. Sohn, *et al.*, “Parametric control of flexible timing through low-dimensional neural manifolds,” *Neuron*, vol. 111, no. 5, 739–753.e8, 2023.
- [7] D. Sussillo and O. Barak, “Opening the black box: low-dimensional dynamics in high-dimensional recurrent neural networks,” *Neural Comput.*, vol. 25, no. 3, pp. 626–649, 2013.
- [8] L. Duncker and M. Sahani, “Dynamics on the manifold: Identifying computational dynamical activity from neural population recordings,” *Curr. Opin. Neurobiol.*, vol. 70, pp. 163–170, 2021.
- [9] J. A. Gallego, M. G. Perich, L. E. Miller, *et al.*, “Neural manifolds for the control of movement,” *Neuron*, vol. 94, no. 5, pp. 978–984, 2017.
- [10] P. T. Toi, H. J. Jang, K. Min, *et al.*, “In vivo direct imaging of neuronal activity at high spatiotemporal resolution,” *Science*, vol. 378, no. 6616, pp. 160–168, 2022.

- [11] N. A. Steinmetz, C. Aydin, A. Lebedeva, *et al.*, “Neuropixels 2.0: A miniaturized high-density probe for stable, long-term brain recordings,” *Science*, vol. 372, no. 6539, eabf4588, 2021.
- [12] V. Villette, M. Chavarha, I. K. Dimov, *et al.*, “Ultrafast two-photon imaging of a high-gain voltage indicator in awake behaving mice,” *Cell*, vol. 179, no. 7, 1590–1608.e23, 2019.
- [13] J. Lauer, M. Zhou, S. Ye, *et al.*, “Multi-animal pose estimation, identification and tracking with DeepLabCut,” *Nat. Methods*, vol. 19, no. 4, pp. 496–504, 2022.
- [14] T. D. Pereira, N. Tabris, A. Matsliah, *et al.*, “SLEAP: A deep learning system for multi-animal pose tracking,” *Nat. Methods*, vol. 19, no. 4, pp. 486–495, 2022.
- [15] A. Gosztolai, S. Günel, V. Lobato-Ríos, *et al.*, “LiftPose3D, a deep learning-based approach for transforming two-dimensional to three-dimensional poses in laboratory animals,” *Nat. Methods*, vol. 18, no. 8, pp. 975–981, 2021.
- [16] S. L. Brunton, B. W. Brunton, J. L. Proctor, *et al.*, “Chaos as an intermittently forced linear system,” *Nat. Commun.*, vol. 8, no. 1, pp. 1–8, 2017.
- [17] B. Lusch, J. N. Kutz, and S. L. Brunton, “Deep learning for universal linear embeddings of nonlinear dynamics,” *Nat. Commun.*, vol. 9, no. 1, pp. 851–10, 2018.
- [18] T. Kipf, E. Fetaya, K.-C. Wang, *et al.*, “Neural relational inference for interacting systems,” *arXiv preprint arXiv:1802.04687*, 2018.
- [19] C. Pandarinath, D. J. O’Shea, J. Collins, *et al.*, “Inferring single-trial neural population dynamics using sequential auto-encoders,” *Nat. Methods*, pp. 1–21, 2018.
- [20] F. Zhu, H. A. Grier, R. Tandon, *et al.*, “A deep learning framework for inference of single-trial neural population dynamics from calcium imaging with subframe temporal resolution,” *Nat. Neurosci.*, vol. 25, no. 12, pp. 1724–1734, 2022.
- [21] O. Yair, R. Talmon, R. R. Coifman, *et al.*, “Reconstruction of normal forms by learning informed observation geometries from data,” *Proc. Natl. Acad. Sci. U. S. A.*, vol. 114, no. 38, E7865–E7874, 2017.
- [22] M. Dabagia and P. Konrad, “Comparing high-dimensional neural recordings by aligning their low-dimensional latent representations,” *Nat. Biomed. Eng.*, pp. 1–16, 2021.
- [23] S. Schneider, J. H. Lee, and M. W. Mathis, “Learnable latent embeddings for joint behavioral and neural analysis,” *CoRR*, vol. abs/2204.00673, 2022.
- [24] G. Sugihara and R. M. May, “Nonlinear forecasting as a way of distinguishing chaos from measurement error in time series,” *Nature*, vol. 344, no. 6268, pp. 734–741, 1990.
- [25] G. Sugihara, R. May, H. Ye, *et al.*, “Detecting causality in complex ecosystems,” *Science (80-.)*, vol. 338, no. 6106, pp. 496–500, 2012.
- [26] A. Gosztolai and A. Arnaudon, “Unfolding the multiscale structure of networks with dynamical Ollivier-Ricci curvature,” *Nat. Commun.*, vol. 12, no. 1, p. 4561, 2021.
- [27] D. J. Skinner, B. Song, H. Jeckel, *et al.*, “Topological metric detects hidden order in disordered media,” *Phys. Rev. Lett.*, vol. 126, no. 4, p. 48101, 2021.
- [28] M. M. Bronstein, J. Bruna, Y. Lecun, *et al.*, “Geometric Deep Learning: Going beyond Euclidean data,” *IEEE Signal Process. Mag.*, vol. 34, no. 4, pp. 18–42, 2017.
- [29] J. Masci, D. Boscaini, M. M. Bronstein, *et al.*, “Geodesic convolutional neural networks on riemannian manifolds,” in *2015 IEEE International Conference on Computer Vision Workshop (ICCVW)*, Los Alamitos, CA, USA: IEEE Computer Society, 2015, pp. 832–840.
- [30] M. M. Bronstein, J. Bruna, T. Cohen, *et al.*, *Geometric deep learning: Grids, groups, graphs, geodesics, and gauges*, 2021.
- [31] D. Grattarola and P. Vandergheynst, “Generalised implicit neural representations,” *Advances in Neural Information Processing Systems*, 2022.
- [32] E. Jenner and M. Weiler, “Steerable partial differential operators for equivariant neural networks,” in *International Conference on Learning Representations*, 2022.
- [33] D. Floryan and M. D. Graham, “Data-driven discovery of intrinsic dynamics,” *Nat. Mach. Intell.*, vol. 4, no. 12, pp. 1113–1120, 2022.

- [34] N. Sharp, S. Attaiki, K. Crane, *et al.*, “DiffusionNet : discretization agnostic learning on surfaces,” *ACM Trans. Graph.*, vol. 99, no. 99, 2020.
- [35] D. Beaini, S. Passaro, V. Létourneau, *et al.*, “Directional graph networks,” in *International Conference on Machine Learning*, PMLR, 2021, pp. 748–758.
- [36] C. Bodnar, F. D. Giovanni, B. P. Chamberlain, *et al.*, “Neural sheaf diffusion: A topological perspective on heterophily and oversmoothing in GNNs,” in *Advances in Neural Information Processing Systems*, A. H. Oh, A. Agarwal, D. Belgrave, *et al.*, Eds., 2022.
- [37] W. L. Hamilton, R. Ying, and J. Leskovec, “Inductive representation learning on large graphs,” *Adv. Neural Inf. Process. Syst.*, vol. 2017-Decem, no. Nips, pp. 1025–1035, 2017.
- [38] C. Fefferman, S. Mitter, and H. Narayanan, “Testing the manifold hypothesis,” *Journal of the American Mathematical Society*, vol. 29, no. 4, pp. 983–1049, 2016.
- [39] L. McInnes, J. Healy, N. Saul, *et al.*, “Umap: Uniform manifold approximation and projection,” *The Journal of Open Source Software*, vol. 3, no. 29, p. 861, 2018.
- [40] T. Flesch, K. Juechems, T. Dumbalska, *et al.*, “Orthogonal representations for robust context-dependent task performance in brains and neural networks,” *Neuron*, vol. 110, no. 7, 1258–1270.e11, 2022.
- [41] R. Rajalingham, A. Piccato, and M. Jazayeri, “Recurrent neural networks with explicit representation of dynamic latent variables can mimic behavioral patterns in a physical inference task,” *Nat. Commun.*, vol. 13, no. 1, 2022.
- [42] A. R. Galgali, M. Sahani, and V. Mante, “Residual dynamics resolves recurrent contributions to neural computation,” *Nat. Neurosci.*, 2023.
- [43] S. Kornblith, M. Norouzi, H. Lee, *et al.*, “Similarity of neural network representations revisited,” *36th Int. Conf. Mach. Learn. ICML 2019*, vol. 2019-June, pp. 6156–6175, 2019.
- [44] A. H. Williams, E. Kunz, S. Kornblith, *et al.*, “Generalized shape metrics on neural representations,” *Adv. Neural Inf. Process. Syst.*, vol. 6, no. NeurIPS, pp. 4738–4750, 2021.
- [45] Y. Miyashita, “Neuronal correlate of visual associative long-term memory in the primate temporal cortex,” *Nature*, vol. 335, no. 6193, pp. 817–820, 1988.
- [46] A. Dubreuil, A. Valente, M. Beiran, *et al.*, “The role of population structure in computations through neural dynamics,” *Nat. Neurosci.*, vol. 25, no. 6, pp. 783–794, 2022.
- [47] F. Mastrogiovanni and S. Ostoicic, “Linking Connectivity, Dynamics, and Computations in Low-Rank Recurrent Neural Networks,” *Neuron*, vol. 99, no. 3, 609–623.e29, 2018.
- [48] J. Kalaska, R. Caminiti, and A. Georgopoulos, “Cortical mechanisms related to the direction of two-dimensional arm movements: Relations in parietal area 5 and comparison with motor cortex,” *Experimental Brain Research*, vol. 51, no. 2, pp. 247–260, 1983.
- [49] A. Gosztolai and P. Ramdya, “Connecting the dots in ethology: applying network theory to understand neural and animal collectives,” *Curr. Opin. Neurobiol.*, vol. 73, p. 102532, 2022.

Supplementary material

1 The MARBLE method

The MARBLE method aims to find a similarity-preserving map from the local vector field features to a shared latent space. Since the method processes vector fields point-by-point, it suffices to describe it applied to a single vector field and the generalisation to the joint embedding of multiple vector fields is straightforward.

Given a smooth, compact m -dimensional manifold \mathcal{M} described by a point cloud $\mathbf{X} = (\mathbf{x}_1, \dots, \mathbf{x}_n)$, MARBLE aims at representing a set of vector fields $\mathbf{F} = \{\mathbf{f}_1, \dots, \mathbf{f}_n\}$ on this manifold as an empirical distribution $P(\mathbf{Z}) = \sum_{i=0}^n \delta(\mathbf{z}_i)$ on a latent space with coordinates $\mathbf{Z} = (\mathbf{z}_1, \dots, \mathbf{z}_n)$. Such vector fields can be obtained from time-series data with for example first-order finite difference $\mathbf{f}_i := \mathbf{x}(t_i+1) - \mathbf{x}(t_i)$. For a chosen set of points on this manifold, we obtain their latent space coordinates \mathbf{Z} from the vector field restricted to a neighbourhood around each point with an unsupervised learning architecture.

The resulting statistical distribution P_c on the latent space then represents reduced information about the underlying dynamical system. If subsets of points belonging to different dynamical systems are considered together, the embedding can be used to disentangle differences in their dynamics, while being invariant, or not to the geometry encoded in the manifold.

1.1 Approximating the manifold by a proximity graph

To define the local neighbourhood on \mathcal{M} , we describe it with a proximity graph. To obtain a faithful representation of the tangent space of \mathcal{M} via the finite difference vector fields \mathbf{F} , we need to ensure that the graph is as homogeneous as possible. In particular, if points come from dynamical trajectories, taking consecutive temporal points should be prohibited. For this reason, we generate the proximity graph from a subsample of points obtained by farthest point sampling [1], with a criterion $\beta \in [0, 1]$ that controls the spacing of the points relative to the diameter of the manifold $\max_{ij}(\|\mathbf{x}_i - \mathbf{x}_j\|_2) < \beta \text{diam}(\mathcal{M})$.

Then, several classical proximity graph algorithms can be used, such as the k -NN algorithm and the ϵ -ball algorithm, but we found that the continuous k -nearest neighbour (ck -NN) algorithm [2] creates more representative neighbourhoods. Indeed, contrary to the classical k -NN graph algorithm, it can be interpreted as a local kernel density estimate and accounts for sampling density variations over \mathcal{M} . The ck -NN algorithm extends the classical k -NN algorithm by accounting for density variations by connecting i and j whenever $\|\mathbf{x}_i - \mathbf{x}_j\|_2^2 < \delta \|\mathbf{x}_i - \mathbf{x}_u\|_2 \|\mathbf{x}_j - \mathbf{x}_v\|_2$, where $\delta > 0$ is a scaling parameter, u, v are the k -th nearest neighbours of i, j , respectively, and $\|\cdot\|_2$ is the Euclidean norm.

This proximity graph endows \mathcal{M} with a geodesic structure, i.e., for any $i, j \in \mathcal{M}$ there is a shortest path with distance $d(i, j)$. We can then define the local neighbourhood as p -hop geodesic neighbourhood $\mathcal{N}(i, p)$ around each point i , restrict the vector field to it and define *local features* at each point.

1.2 Parametrising the tangent spaces

Unlike \mathbb{R}^m , the tangent spaces of \mathcal{M} do not come with a preferred coordinate system. However, being isomorphic to \mathbb{R}^m , they can be parametrised by a family of local orthogonal coordinate frames, also known as gauges, whose components are \mathbb{R}^d -valued vectors. Specifically, we assume that the tangent space at a node i , $\mathcal{T}_i \mathcal{M}$, is spanned by the edge vectors $\mathbf{e}_{ij} \in \mathbb{R}^d$ pointing from i to K nodes j in its neighbourhood on the proximity graph. The m largest singular values $\mathbf{t}_i^{(\cdot)} \in \mathbb{R}^d$ of the matrix formed by column-stacking \mathbf{e}_{ij} yield the orthonormal coordinate frame $\mathbb{T}_i \in \mathbb{R}^{d \times m} = (\mathbf{t}_i^{(1)}, \dots, \mathbf{t}_i^{(m)})$ spanning $\mathcal{T}_i \mathcal{M}$. In practice, we pick $K > \text{deg}(i)$ closest nodes to i on the proximity graph where K is a hyperparameter. Larger K increases the overlaps between the nearby tangent spaces and we find that $K = 2|\mathcal{N}(i, 1)|$ is often a good compromise between locality and robustness to noise of the tangent space approximation. Note that because \mathbb{T}_i defines an orthogonal basis $\mathbb{T}_i^T \mathbf{f}_i$ acts as a projection of the signal to the tangent space in the ℓ_2 sense. We perform these computations using a modified version of the Parallel Transport Unfolding package [3]. For illustration, we display the computed frames on a spherical manifold (Fig. 4).

1.3 Connections between tangent spaces

Having the local frames, we next define the parallel transport map $\mathcal{P}_{j \rightarrow i}$ aligning the local frame at j to that at i , which is necessary to define convolution operations in a common space. While parallel transport is generally path dependent, we assume that adjacent nodes i, j are close enough to consider the unique smallest rotation, known as the Lévy-Civita connection. Thus, for adjacent edges, $\mathcal{P}_{j \rightarrow i}$ can be computed as the matrix \mathbf{O}_{ji} corresponding to $\mathcal{P}_{j \rightarrow i}$, as the orthogonal transformation (rotation and reflection)

$$\mathbf{O}_{ji} = \arg \min_{\mathbf{O} \in O(m)} \|\mathbb{T}_i - \mathbb{T}_j \mathbf{O}\|_F, \quad (1)$$

where $\|\cdot\|_F$ is the Frobenius norm. The unique solution to this problem is found by the Kabsch algorithm [4].

Note that \mathbb{T}_i is defined only up to an orthogonal transformation (rotation and reflection) within the tangent space of \mathcal{M} because the m -dimensional $\mathcal{T}_i \mathcal{M}$ only constrains m coordinates of the frame. However, when the signal is projected to the local frame, the tangent frame alignment by $\mathcal{P}_{j \rightarrow i} = \mathbf{O}_{ij}$ removes this ambiguity. Indeed, suppose that each node carries the same signal \mathbf{f} . Then, parallel transport alignment of the projected signal from j to i yields

$$\mathbb{T}_i^T \mathbf{f} = \mathbf{O}_{ij} \mathbb{T}_j^T \mathbf{f} = (\mathbb{T}_j \mathbf{O}_{ji})^T \mathbf{f} = \mathbb{T}_i^T \mathbf{f}, \quad (2)$$

where in the first equality used the definition of the parallel transport, the second equality the transpose operation, while the third equality used Eq. (1). Note that the same result does not hold when parallel transporting signals in the ambient space (without projection), because in that case, the ambiguity in the frame orientation introduces ambiguity in the signal

1.4 Vector diffusion

Before constructing the local vector field features, we use a vector diffusion layer to smooth out noisy vector field samples. Vector diffusion is a generalisation of the scalar (heat) diffusion, and can be expressed as a kernel associated with the vector diffusion equation [5] to produce a smoothed vector field

$$\text{vec}(\mathbf{F}(\tau)) = e^{-\tau \mathcal{L}} \text{vec}(\mathbf{F}). \quad (3)$$

where $\text{vec}(\mathbf{F}) \in \mathbb{R}^{nd \times 1}$ the row-wise concatenation of vector-valued signals, τ is a learnable parameter that controls the scale of the features and \mathcal{L} is the random-walk normalised connection Laplacian defined as a block matrix whose nonzero blocks are given by

$$\mathcal{L}(i, j) = \begin{cases} \mathbf{I}_{m \times m} & \text{for } i = j \\ -\text{deg}(i)^{-1} \mathbf{O}_{ij} & \text{for } j \in \mathcal{N}(i, 1). \end{cases} \quad (4)$$

See Ref. [6] for further details. Intuitively, rather than diffusion of the vectors component-wise, vector diffusion smoothens vectors based on differences between a vector at a given node and other vectors parallel transported to this node.

1.5 Gradient filters

Before we can learn the local features of the vector field, we define gradient filters, whose role is to approximate the variation of the vector field around a point in the local tangent frame. To numerically compute the gradient at a point $i \in \mathcal{M}$ we construct an anisotropic filter by extending the directional derivative filter of Beaini et al. [7] using local coordinates. To do so, consider the local frame \mathbb{T}_i and construct the directional derivative filter in the direction of the q -th unit vector $\mathbf{t}_i^{(q)}$. We follow Beaini et al. and decompose $\mathbf{t}_i^{(q)} \in \mathbb{R}^{d \times 1}$ by projecting it to the set of edge vectors \mathbf{e}_{ij} to obtain a vector $\hat{\mathbf{t}}_i^{(q)} \in \mathbb{R}^{n \times 1}$ at node i pointing in the basis direction q with components j

$$\hat{\mathbf{t}}_i^{(q)}(j) = \begin{cases} \langle \mathbf{t}_i^{(q)}, \mathbf{e}_{ij} \rangle / \text{deg}(i) & \text{if } j \in \mathcal{N}(i, 1) \\ 0 & \text{otherwise.} \end{cases} \quad (5)$$

Collating for all nodes, we can write a matrix for the q -th coordinate of the local frame projected onto the edge vectors $\widehat{\mathbb{T}}_q = (\widehat{\mathbf{t}}_1^{(q)}, \dots, \widehat{\mathbf{t}}_n^{(q)}) \in \mathbb{R}^{n \times n}$. Using this decomposition, the directional derivative of the scalar field s_i at i in the direction \mathbf{t}_i^q is given by

$$\mathcal{K}^{(i,q)} s_i := \langle \nabla s_i, \widehat{\mathbf{t}}_i^{(q)} \rangle = \sum_{j \in \mathcal{N}(i,1)} (s_j - s_i) \widehat{t}_i^{(q)}(j). \quad (6)$$

or in matrix form

$$\mathbf{K}^{(q)} \mathbf{s} = (\widehat{\mathbb{T}}_q - \text{diag}(\widehat{\mathbb{T}}_q \mathbf{1}_n)) \mathbf{s}, \quad (7)$$

where $\mathbf{1}_n$ is the $n \times 1$ vector of ones. As a result, the gradient of a scalar field can then be obtained by column-wise concatenating (as new channels) the derivatives against all directions in the basis set

$$\nabla \mathbf{s} = (\mathcal{D}^{(1)} \mathbf{s}, \dots, \mathcal{D}^{(d)} \mathbf{s}). \quad (8)$$

Figs. 5a,b show the output of the first and second-order filters applied to a linear and a quadratic scalar field.

To compute the component-wise directional derivative for a vector field $\mathbf{F} \in \mathbb{R}^{n \times m}$, one must first parallel transport the local frames at the neighbours j to i before applying the anisotropic filters in Eq. (7). Let \mathbf{O} denote the $nm \times nm$ block matrix of $m \times m$ blocks given by the connection matrices \mathbf{O}_{ij} . Then, we may express Eq. (12) in matrix form as

$$\mathcal{D}^{(q)} \mathbf{F} = ((\mathbf{K}^{(q)} \otimes \mathbf{1}_m^T \mathbf{1}_m) \odot \mathbf{O}) \mathbf{F}, \quad (9)$$

Here the kronecker product in the inner brackets expands $\mathbf{K}^{(q)}$ to the $nm \times nm$ block matrix where the (i, j) $m \times m$ block is filled with entries $K_{ij}^{(q)}$.

1.6 Approximating the local features

We now define convolution kernels on \mathcal{M} that act on the vector field to give a representation of the feature at a given point. We first project the vector signal to the manifold $\mathbf{f}'_i = \mathbb{T}_i^T \mathbf{f}_i$. This reduces the dimension of \mathbf{f}_i from d to m without losing information since \mathbf{f}_i was already in the tangent space. We drop the bar in the sequel to understand that all vectors are expressed in local coordinates. In this local frame, the best polynomial approximation of the vector field around i is given by the Taylor-series expansion of each component $f_{i,l}$ of \mathbf{f}_i

$$f_{j,l} \approx f_{i,l} + \nabla f_{i,l}(\mathbf{x}_j - \mathbf{x}_i) + \frac{1}{2} (\mathbf{x}_j - \mathbf{x}_i)^T \nabla^2 f_{i,l}(\mathbf{x}_j - \mathbf{x}_i) + \dots \quad (10)$$

Motivated by the Taylor approximation, we construct gradient operators of increasing order to describe the vector field features. We implement the gradient operators as a set of m anisotropic filters $\{\mathcal{D}^{(q)}\}$ acting along $\{\mathbf{t}_i^{(q)}\}$,

$$\nabla f_{i,l} \approx \left(\mathcal{D}^{(1)}(f_{i,l}), \dots, \mathcal{D}^{(m)}(f_{i,l}) \right)^T, \quad (11)$$

where $\mathcal{D}^{(q)}(f_{i,l})$ is the l -th component of

$$\mathcal{D}^{(q)}(\mathbf{f}_i) = \sum_{j=1}^n \mathcal{K}_j^{(i,q)} \mathcal{P}_{j \rightarrow i}(\mathbf{f}_j) \quad (12)$$

where $\mathcal{P}_{j \rightarrow i} = \mathbf{O}_{ij}$ is the parallel transport operator that takes the vector \mathbf{f}_j from the adjacent frame j to a common frame at i and $\mathcal{K}^{(i,q)} \in \mathbb{R}^{n \times n}$ is a directional derivative filter [7] (Eq. (7)) expressed in local coordinates at i and acting along $\mathbf{t}_i^{(q)}$. As a result of the parallel transport, the value of Eq. (12) is independent of the local curvature of the manifold. The p -th order gradients can be defined by the iterated application of the filters, which aggregates information in the p -hop neighbourhood of points. Although we find that increasing the order of the differential operators increases the expressiveness of the network (Fig. 6), second-order filters ($p = 2$) were sufficient for the application considered in this paper.

The expansion in Eq. (10) suggests augmenting the vectors \mathbf{f}_i by the derivatives (Eq. (11)), to obtain a matrix

$$\mathbf{f}_i \mapsto \mathbf{f}_i^{\mathcal{D}} = (\mathbf{f}_i, \nabla f_{i,1}, \dots, \nabla f_{i,m}, \nabla(\nabla f_{i,1})_1, \dots, \nabla(\nabla f_{i,m})_m), \quad (13)$$

of dimensions $m \times c$ whose columns are gradients of signal components up to order p to give a total of $c = (1 - m^{p+1})/(m(1 - m))$ vectorial channels.

1.7 Inner product for geometry invariance

In the optional geometry-agnostic mode, we note that deformation on the manifold have the effect of introducing rotations into the local features. Thus, we can achieve invariance to these deformations by making the learnt features rotation invariant. We do so by transforming the $m \times c$ matrix \mathbf{f}_i^D to a $1 \times c$ vector

$$\mathbf{f}_i^D \mapsto \mathbf{f}_i^{ip} = \left(\mathcal{E}^{(1)}(\mathbf{f}_i^D), \dots, \mathcal{E}^{(c)}(\mathbf{f}_i^D) \right), \quad (14)$$

by taking for each channel the inner product against all other channels, weighted by a dense learnable matrix $\mathbf{A}^{(r)} \in \mathbb{R}^{m \times m}$ and summing,

$$\mathcal{E}^{(r)}(\mathbf{f}_i^D) = \mathcal{E}^{(r)}(\mathbf{f}_i^D; \mathbf{A}^{(r)}) := \sum_{s=1}^c \left\langle \mathbf{f}_i^D(\cdot, r), \mathbf{A}^{(r)} \mathbf{f}_i^D(\cdot, s) \right\rangle, \quad (15)$$

for $r = 1, \dots, c$ (Fig. 1f). Taking inner products is valid because the columns of \mathbf{f}_i^D all live in the tangent space at i . Intuitively, Eq. (15) achieves coordinate independence by learning rotation and scaling relationships between pairs of channels.

1.8 Embedding with MLP

To embed each local feature, \mathbf{f}_i^{ip} or \mathbf{f}_i^D , depending on if inner product features are used, (Eq. (14)) we use a multilayer perceptron (MLP) (Fig. 1g)

$$\mathbf{z}_i = \text{MLP}(\mathbf{f}_i^{ip}; \omega), \quad (16)$$

where ω are trainable weights. The MLP is composed of L linear (fully-connected) layers interspersed by ReLU non-linearities. We used $L = 2$ with a sufficiently high output dimension to encode the variables of interest. The parameters were initialised using Kaiming method [8].

1.9 Loss function

Unsupervised training of the network is possible due to the continuity in the vector field over \mathcal{M} , which causes nearby features to be more similar than distant features. We implement this via negative sampling [9], which uses random walks sampled at each node to embed neighbouring points on the manifold close together while pushing points sampled uniformly at random far away. We use the following unsupervised loss function from Hamilton et al. [9]:

$$\mathcal{J}(\mathbf{Z}) = -\log(\sigma(\mathbf{z}_i^T \mathbf{z}_j)) - Q \mathbb{E}_{k \sim U(n)} \log(\sigma(-\mathbf{z}_i^T \mathbf{z}_k)). \quad (17)$$

where $\sigma(x) = (1 + e^{-x})^{-1}$ is the sigmoid function and $U(n)$ is the uniform distribution over the n nodes. To compute this function, we sample one-step random walks from every node i to obtain 'positive' node samples for which we expect similar features to that of node i . The first term in Eq. (17) seeks to embed these nodes close together. At the same time, we also sample nodes uniformly at random to obtain 'negative' node samples with likely different features from that of node i . The second term in Eq. (17) seeks to embed these nodes far away. We choose $Q = 1$.

We optimise the loss Eq. (17) by stochastic gradient descent. For training, the nodes from all manifolds were randomly split into training (80%), validation (10%) and test (10%) sets. The optimiser was run until convergence of the validation set and the final results were tested on the test set with the optimised parameters.

1.10 Pseudo code of MARBLE algorithm

We implemented MARBLE architecture with Pytorch Geometric [10]. The general algorithm is as follows.

Algorithm 1 MARBLE

Input: d -dimensional vector field samples $\mathbf{F} = (\mathbf{f}_1, \dots, \mathbf{f}_n)$
 connection Laplacian \mathcal{L}
 derivative filters $\mathcal{D}_i^{(q)}$ for $i \in \{1, \dots, n\}$ and $q \in \{1, \dots, m\}$
 derivative order p

Output: Embedding \mathbf{z}_i for all $i \in \{1, \dots, n\}$

| | |
|---|-------------------------------------|
| $\mathbf{F} \leftarrow e^{\tau \mathcal{L}} \mathbf{F}$ | ▷ Apply diffusion layer (optional) |
| $\mathbf{h}^{(0)} \leftarrow \mathbf{f}_i$ | |
| for $1 \leq l \leq p$ do | ▷ Loop over filter orders |
| $\nabla h_q^{(l)} = \left(\mathcal{D}^{(1)}(h_q^{(l)}), \dots, \mathcal{D}^{(m)}(h_q^{(l)}) \right)^T$ | ▷ Compute filters |
| $\mathbf{h}^{(l)} \leftarrow \text{concat} \left(\mathbf{h}^{(l-1)}, \nabla h_1^{(l)}, \dots, \nabla h_m^{(l)} \right)$ | ▷ Concatenate derivatives |
| end for | |
| $\mathbf{h}^{(l)} \leftarrow (\mathcal{E}_1(\mathbf{h}^{(l)}; \mathbf{A}_1), \dots, \mathcal{E}_c(\mathbf{h}^{(l)}; \mathbf{A}_c))$ | ▷ Inner product features (optional) |
| $\mathbf{z}_i \leftarrow \text{MLP}(\mathbf{h}^{(l)}; \omega)$ | ▷ Pass through MLP |

2 Distributional distance between latent representations

To test whether shifts in the statistical representation of the dynamical system can predict global phenomena in the dynamics we define a similarity metric between pairs of vector fields $\mathbf{F}_1, \mathbf{F}_2$ in terms of their corresponding embeddings $\mathbf{Z}_1 = (\mathbf{z}_{1,1}, \dots, \mathbf{z}_{n_1,1})$ and $\mathbf{Z}_2 = (\mathbf{z}_{1,1}, \dots, \mathbf{z}_{n_2,1})$. We use the optimal transport (OT) distance between the empirical distributions $P_1 = \sum_i^{n_1} \delta(\mathbf{z}_{i,1}), P_2 = \sum_i^{n_2} \delta(\mathbf{z}_{i,2})$:

$$d(P_1, P_2) = \min_{\gamma} \sum_{uv} \gamma_{uv} \|\mathbf{z}_{u,1} - \mathbf{z}_{v,2}\|_2^2 \quad (18)$$

where γ is the OT plan, a joint probability distribution subject to marginality constraints that $\sum_u \gamma_{uv} = P_2$, $\sum_v \gamma_{uv} = P_1$ and $\|\cdot\|_2$ is the Euclidean distance.

3 Examples

3.1 Van der Pol oscillator on parabola example

We used the following equations to simulate the Van der Pol system:

$$\begin{aligned} \dot{x} &= y \\ \dot{y} &= \mu(1 - x^2)y - x, \end{aligned} \quad (19)$$

parametrised by μ . If $\mu = 0$, the system reduces to the harmonic oscillator, if $\mu < 0$, the system is unstable and if $\mu > 0$, the system is stable and converges to a limit cycle. In addition, we map this two-dimensional system to a parabola as with the map

$$\begin{aligned} x, y &\mapsto x, y, z = \text{parab}(x, y) \\ \dot{x}, \dot{y} &\mapsto \dot{x}, \dot{y}, \dot{z} = \text{parab}(x + \dot{x}, y + \dot{y}) - \text{parab}(x, y), \end{aligned}$$

where $\text{parab}(x, y) = -(\alpha x)^2 - (\alpha y)^2$. For Fig. 1, we trained MARBLE in the geometry-agnostic mode, see Table 3.3 for parameters. In Fig. 9, we illustrate other examples of the application of MARBLE on this system, with different regimes of μ , and randomness in the parabola curvature across μ , demonstrating the difference between geometry-aware and geometry-agnostic modes of MARBLE.

3.2 Low-rank RNNs

We consider low-rank RNNs composed of $N = 500$ rate units in which the activation of the i -th unit is given by

$$\tau \frac{dx_i}{dt} = -x_i + \sum_{j=1}^N J_{ij} \phi(x_j) + \tilde{u}_i(t) + \eta_i(t), \quad x_i(0) = 0 \quad (20)$$

where $\tau = 100$ ms is a time constant, $\phi(x_i) = \tanh(x_i)$ is the firing rate, J_{ij} is the rank-R connectivity matrix, $u_i(t)$ is an input stimulus and $\eta_i(t)$ is a white noise process with zero mean and std 3×10^{-2} . The connectivity matrix can be expressed as

$$\mathbf{J} = \frac{1}{N} \sum_{r=1}^R \mathbf{m}_r \mathbf{n}_r^T \quad (21)$$

for vector pairs $(\mathbf{m}_r, \mathbf{n}_r)$. For the DMS task, the input is of the form

$$\tilde{u}_i(t) = w_{1i}^{\text{in}} u_1(t) + w_{2i}^{\text{in}} u_2(t), \quad (22)$$

where w_{1i}, w_{2i} are coefficients controlling the weight of inputs u_1, u_2 into node i . Finally, the network firing rates are read out to the output as

$$o(t) = \sum_{i=0}^N w_i^{\text{out}} \phi(x_i). \quad (23)$$

To train the networks we followed the procedure in Ref. [11]. The experiments consisted of 5 epochs; a fixation period of length between $100 - 500$ ms chosen uniformly at random, a 500 ms stimulation period, a delay period of length between $500 - 3000$ ms, a 500 ms stimulation period and a 1000 ms decision period. During training, the networks were subjected to the two inputs, whose value varied discontinuously between zero and a non-zero gain during stimulation periods. The networks were trained against a loss function

$$\mathcal{L} = |o(T) - \hat{o}(T)| \quad (24)$$

where T is the length of the trial and $\hat{o}(T) = 1$ when both stimuli were present and -1 otherwise. Coefficient vectors were initially drawn from zero-mean and unit std Gaussian distributions and then optimised. For training, we used the ADAM optimiser [12] with moment decay rates $0.9 - 0.999$ and learning rates $10^{-3} - 10^{-2}$.

We trained MARBLE in geometry-agnostic mode. See Table 3.3 for parameters.

3.3 Macaque hand reaching data

We used publically available [13] electrophysiology data during a centre-out instructed-delay reaching task. The neural activity was recorded using linear multielectrode arrays (V-Probe, 24-channel linear probes) from rhesus macaque motor (M1) and dorsal premotor (PMd) cortices. See Ref. [13] for further details on experimental procedures. Each trial began with the monkey's hand at the centre position, after which one (or more) of the radial targets at 10cm from the centre position were marked visually (target onset). After a variable delay period, one of the radial targets was highlighted indicating the go-cue for reaching. We analysed the 700ms period after the go-cue consisting of a delay followed by the reach. A total of 44 consecutive experimental sessions with a variable number of trials were considered.

For each of the 24 channels of each trial, we extracted the spike trains using the neo package in Python (<http://neuralensemble.org/neo/>) and converted them into instantaneous rates using Gaussian kernel convolution with a standard deviation of 100ms. We then binned the rates at 20ms intervals using the elephant Python package [14] to match the sampling frequency in the decoded kinematics in Ref. [13]. Finally, we fitted a PCA across all trials in a single session to reduce the dimension of the 24-channel rates to five principle components. We trained MARBLE in geometry-aware mode (without inner product features) separately on each individual session, treating each of the seven movement conditions as individual manifolds. See Table 3.3 for parameters.

To decode the hand kinematics from the neural trajectories, we followed same procedure as in Ref. [13]. Specifically, we used Optimal Linear Estimation (OLE) to decode both the x and y reaching

coordinates and velocities from the neural embeddings. For each individual session, using 5-fold cross-validation, we fitted an OLE to map from the MARBLE embeddings to the kinematics. To assess the accuracy of decoded movements, we computed the goodness of fit (R^2) between the decoded and real velocities for both x and y , before taking the mean across them. We also trained a support vector machine classifier (regularisation of 1.0 with a radial basis function) on the real kinematic movements against the known condition labels. We then evaluated the classifier on the decoded kinematics and report the accuracy for each session.

Table 1: Parameters used for MARBLE embedding in the different experiments

| Parameters | Experiment | | |
|------------------------|-------------|--------------|------------------|
| | van der Pol | Low-rank RNN | Macaque reaching |
| Inner product features | True | True | False |
| k | 20 | 15 | 30 |
| Diffusion | False | False | True |
| Feature order, p | 2 | 2 | 2 |
| MLP hidden channels | 32 | 32 | 100 |
| MLP output channels | 5 | 3 | 3 or 20 |
| Number of parameters | 698 | 2886 | 15803 |

4 Supplementary figures

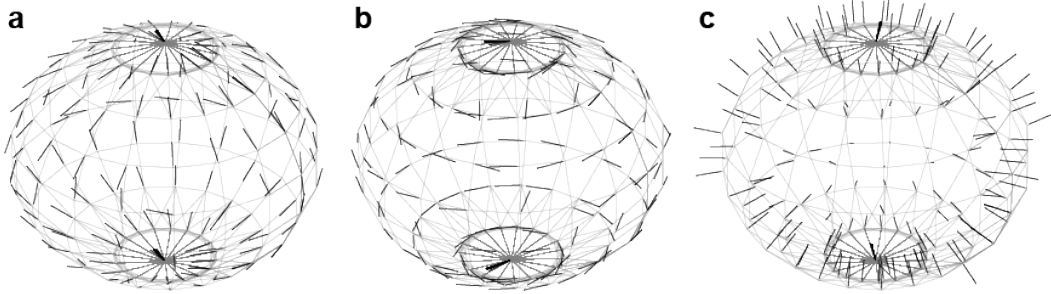


Figure 4: **Illustration of local gauges.** **a,b** Local gauges were fitted to eight neighbours at each point on the rectangular grid over a sphere (manifold of dimension two) embedded into \mathbb{R}^3 . Unit vectors representing within-manifold basis. **c** Unit vector represents normal to the manifold. Note that the orientation of the normal vectors is not necessarily consistent.

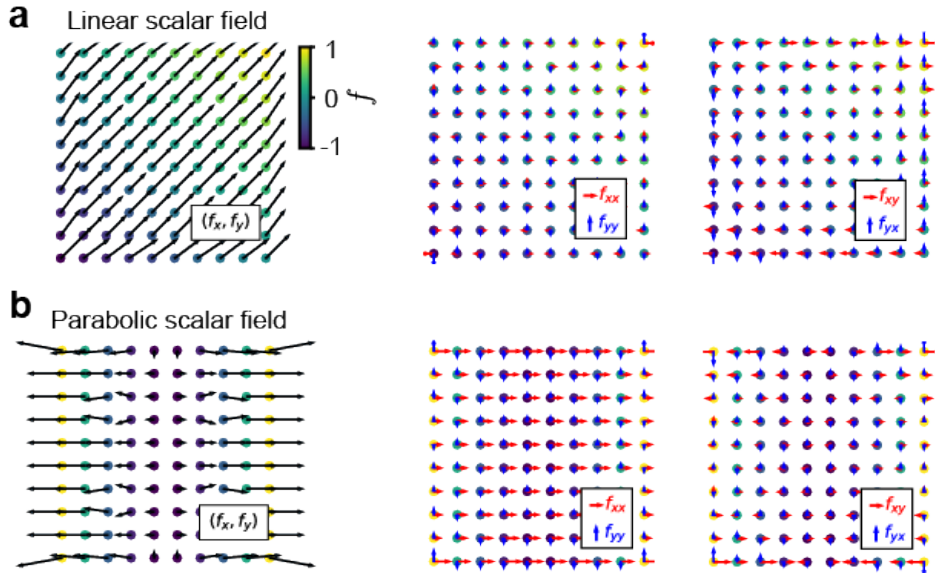


Figure 5: **Output of gradient filters.** **a** Scalar valued linear function. **b** Scalar valued parabolic function. The first column shows the output of the scalar signal convolved with the gradient filter with respect to a principal spatial coordinate, representing the directional (partial) derivatives along this direction. The second and third columns show second-order mixed partial derivatives obtained by a second application of the gradient filter to the derivative signal. In each case, we used a uniform rectangular grid with eight neighbours.

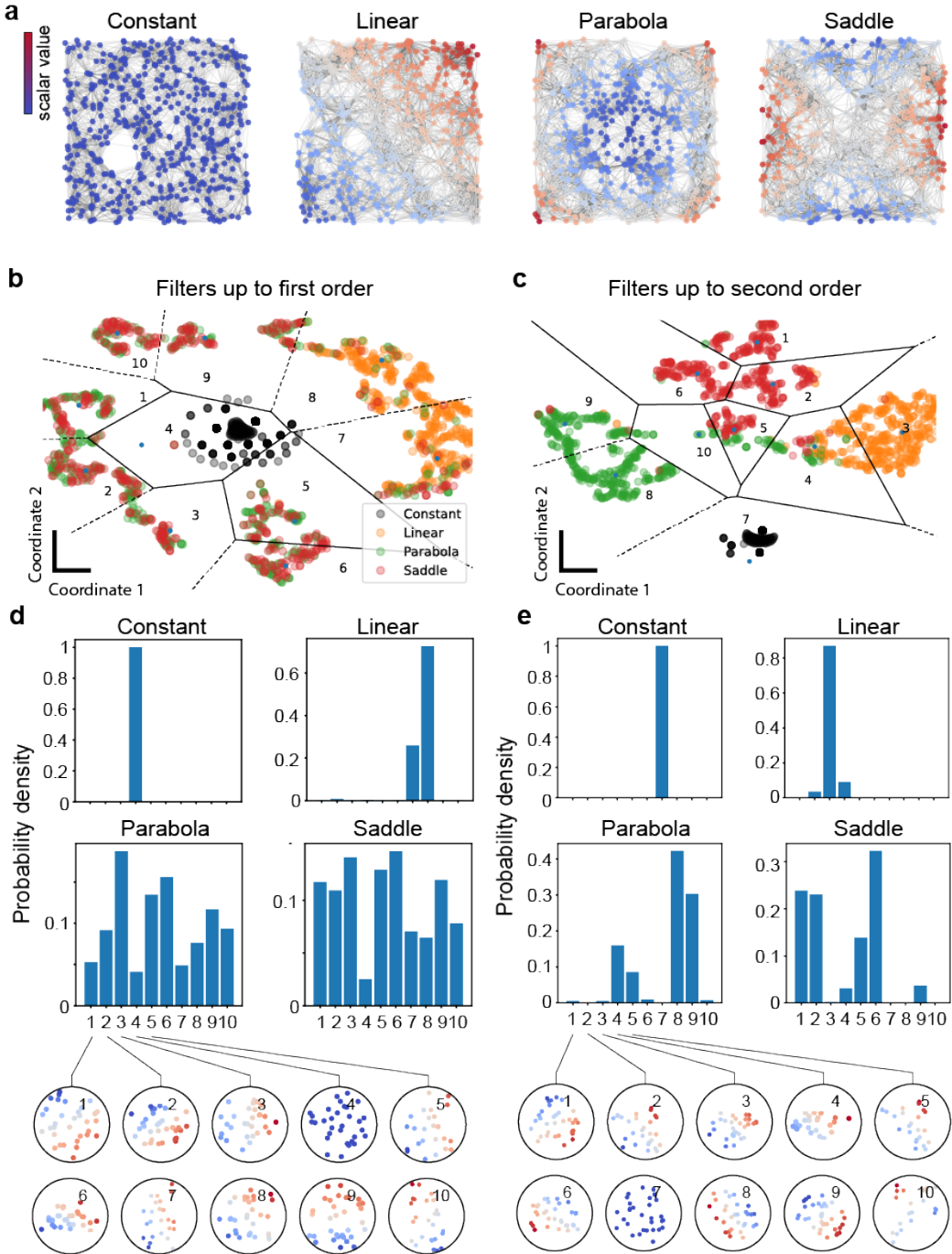


Figure 6: Effect of filter order. **a** Scalar functions sampled ($n = 512$) uniformly at random in the interval $[-1, 1]^2$ and fitted with a continuous k -nearest neighbour graph. From left to right: constant, linear, parabola, saddle. **b** Joint embedding of local features from all functions based on first-order (1-hop) directional derivative filters. Dots represent nodes drawn from **a** with nodes close together signifying similar signal distributions in their neighbourhoods. Black lines show the convex polygon obtained from k -means clustering ($k = 10$). **c** As in **b**, but with first (1-hop) and second-order (2-hop) filters. Including second-order filters increases the clustering of features. **d** Histogram representation of the clustered neighbourhood types. The latter is shown at the bottom in circular insets. **e** As in **d** but with first and second-order filters. Second-order features better discriminate the parabola and saddle but show little difference for constant and linear fields.

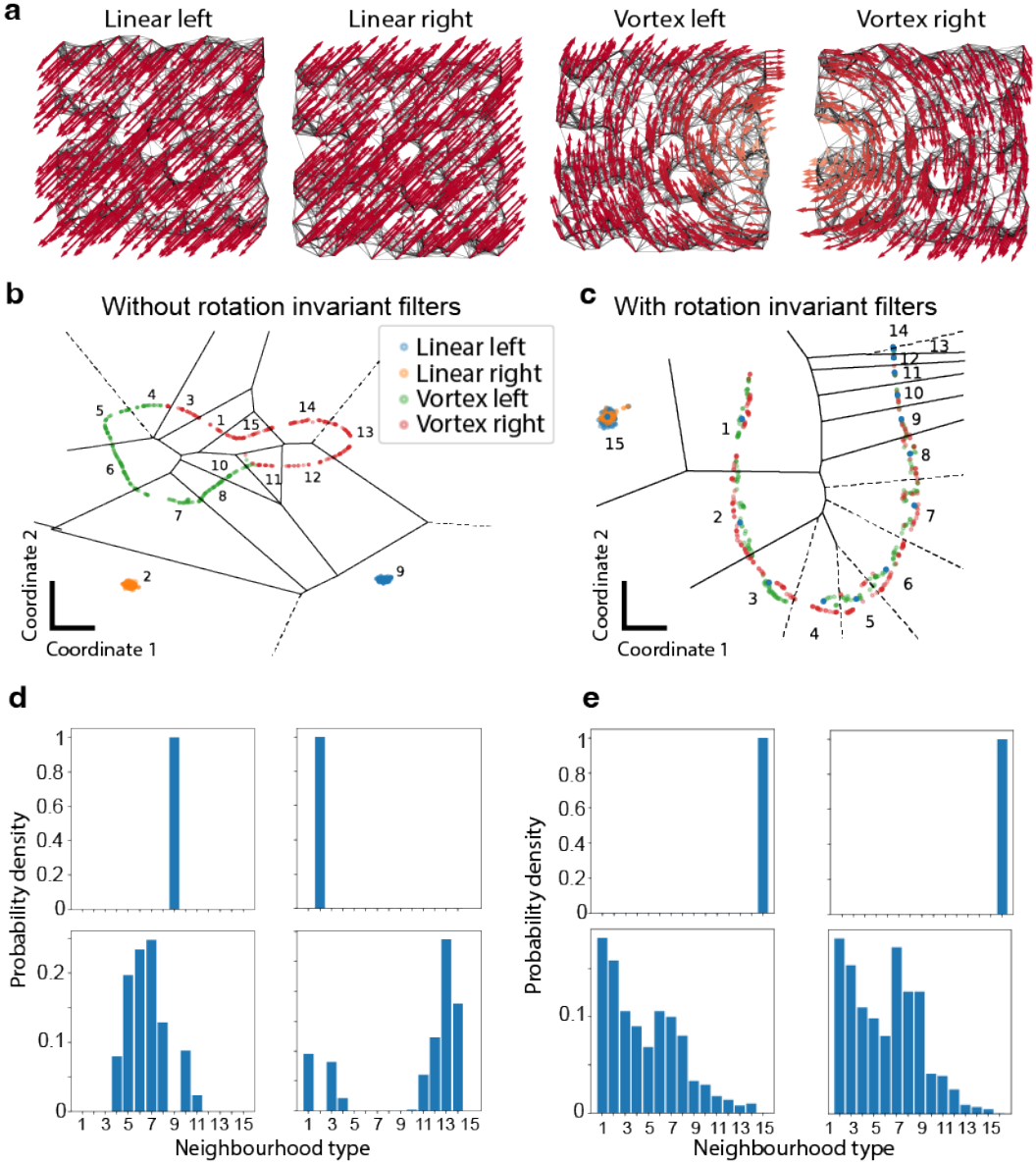


Figure 7: Effect of rotational invariant filters. **a** Vector fields sampled ($n = 512$) uniformly at random in the interval $[-1, 1]^2$ and fitted with a continuous k -nearest neighbour graph. **b** Joint embedding of local features from all functions based on first-order (1-hop) directional derivative filters. Dots represent nodes drawn from **a** with nodes close together signifying similar signal distributions in their neighbourhoods. Features drawn from the linear vector fields cluster together (clusters 2 and 9) while those drawn from the vortex fields fall on separate halves of a 1D circular manifold corresponding to the one-parameter (angle) variation between them. **c** Same as **b** but with rotation invariant features. The features drawn from linear fields can no longer be distinguished (cluster 15) because the filter does not learn the orientation. Features from the vortex fields fall on a linear 1D manifold parametrised by the distance from the centre. **d** The distribution of orientation-preserving derivative features can distinguish all fields. **e** The distribution of rotation-invariant features can discriminate linear fields from vortex fields but not the orientation.

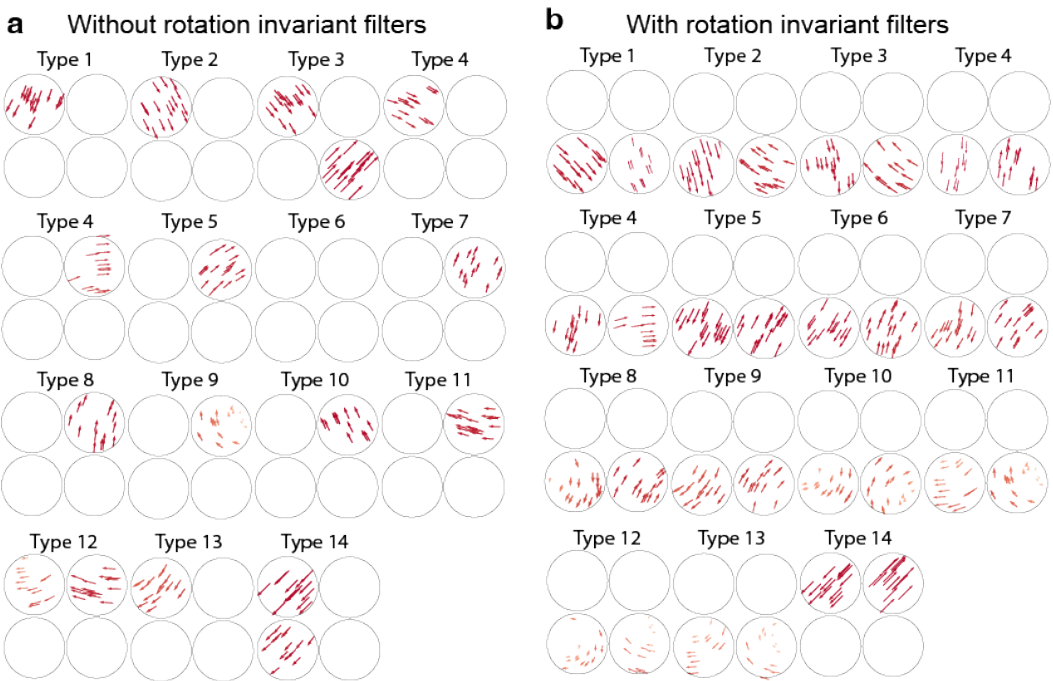


Figure 8: Effect of rotational invariant filters on feature types. Types are feature types with circular insets representing a feature drawn from each of the four fields in Fig. 7. Top left: linear left; top right: linear right; bottom left vortex left; bottom right: vortex right. White insets indicate that the given feature type is not present in the given vector field. **a** Without using rotation invariant filters the network tends to classify features into separate types. **b** With rotation invariant filters, features cluster more irrespective of the orientation. The separate types are instead distinguished more based on the expansion, and rotation properties of the features.

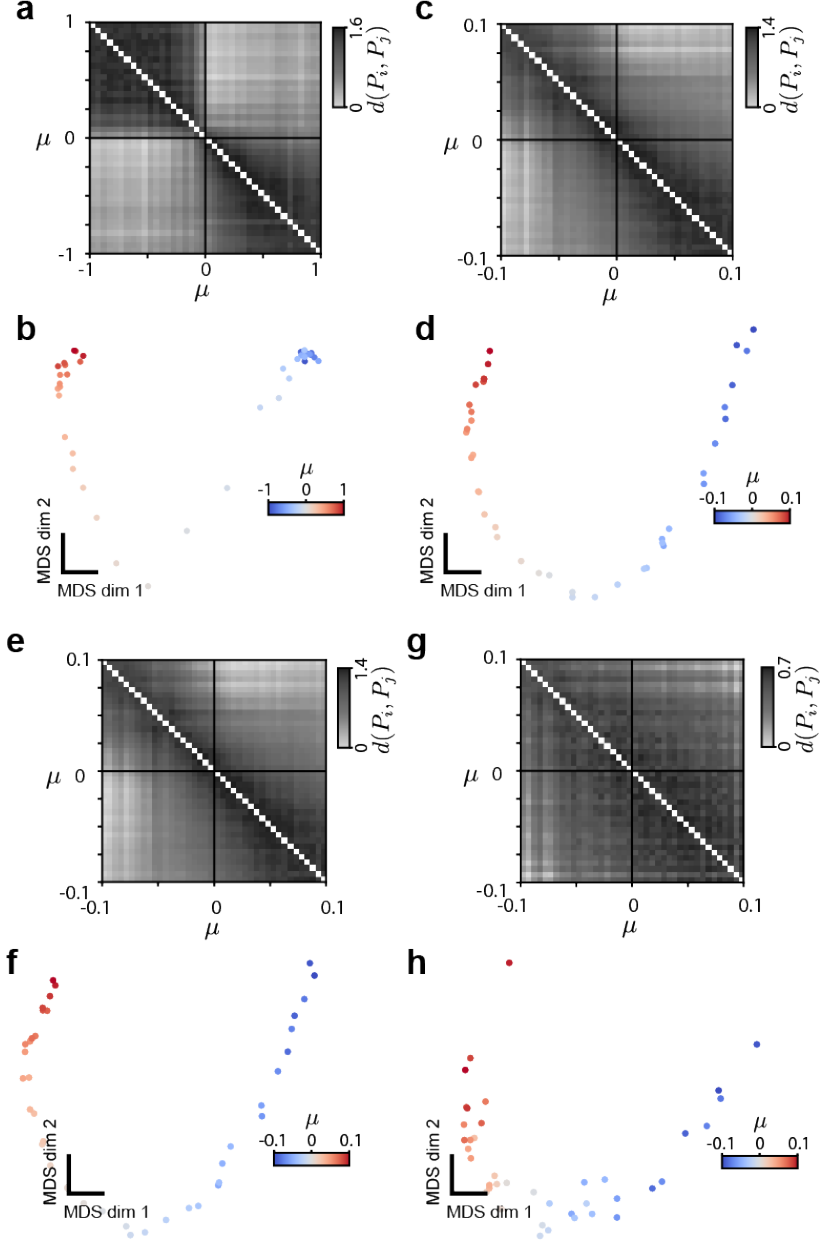


Figure 9: **Additional Van der Pol examples** We illustrate the MARBLE embedding of the Van der Pol example with 40 values of μ in the following cases. **a, b** Larger range of μ from -1 to 1 shows a clear two partition. **c, d** Smaller ranger of μ from -0.1 to 0.1 only shows a band structure. **e, f** Adding noise in the parabola curvature (uniformly from -0.2 to 0.2) with geometry-agnostic mode does not alter the MARBLE embedding. **g, h** Same added noise as in **e, f** but with geometry-aware mode shows a reduction in accuracy to detect the one-dimensional manifold parametrised by μ .

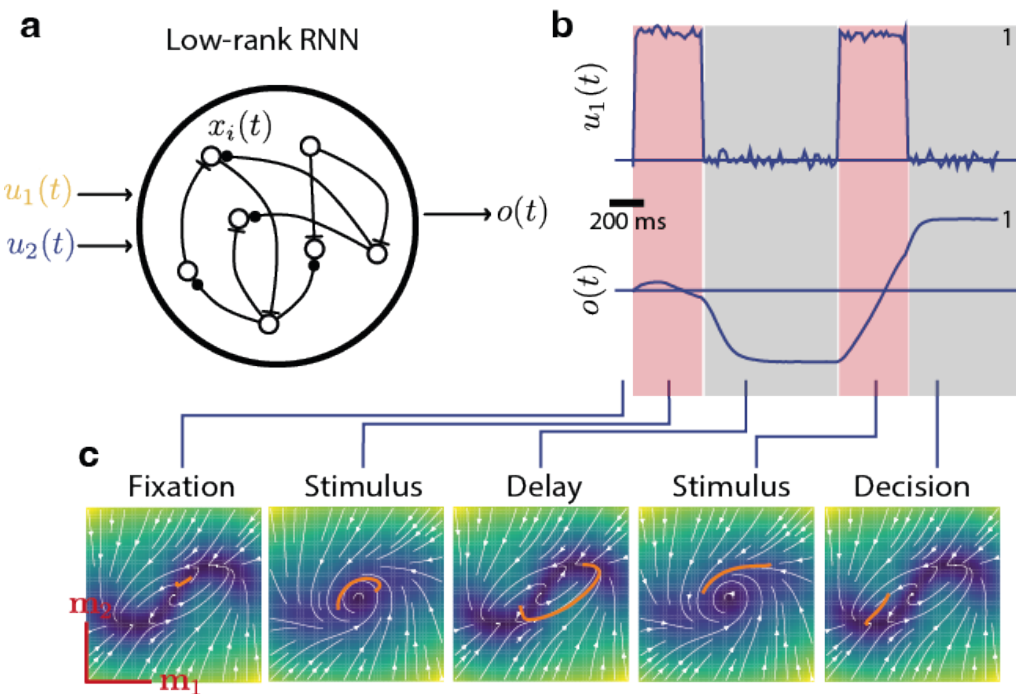


Figure 10: **Neural activities in a rank-2 RNN during the DMS task.** **a** Schematic of a low-rank RNN, taking as input two stimuli and producing a decision variable as output. Arrow endings represent inhibitory and excitatory connections. **b** Two example input pattern for one of the stimuli, and corresponding output pattern. Red and grey-shaded bands show stimulated and unstimulated periods. **c** Mean-field dynamics (heatmap and streamplot) superimposed with a sampled trajectory (orange) during one trial of the DMS task.

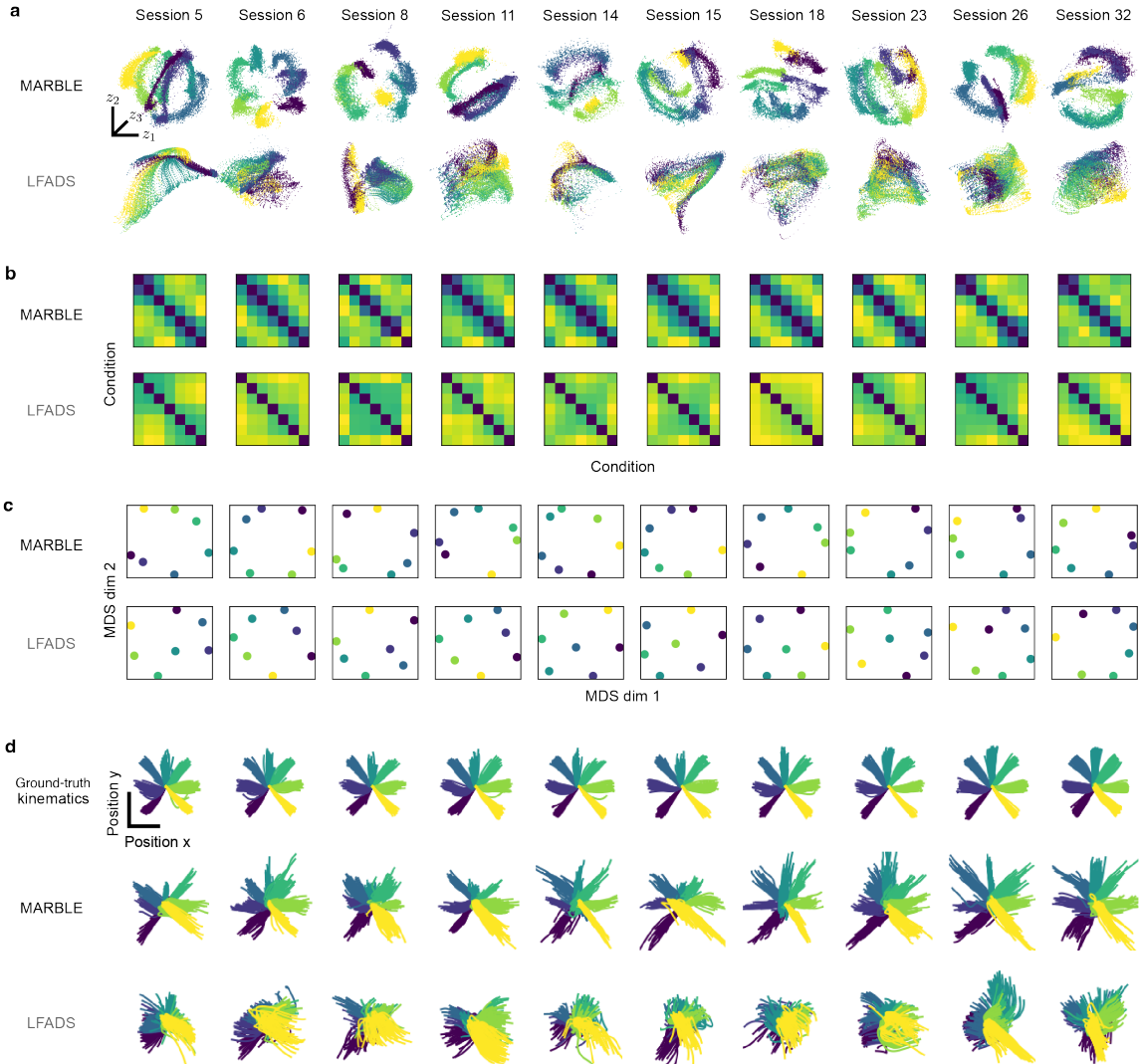


Figure 11: A comparison of MARBLE and LFADS for learning the neural activity for individual sessions of macaque reaching task. **a** Feature embeddings obtained from MARBLE for various example sessions. The 3D-embedded points better reflect the arrangement of reaches in physical space when compared to LFADS. **b** The matrix of distribution distances between pairwise conditions shows stronger periodic structure compared to LFADS. **c** MDS embedding of the distance matrix consistently recovers the spatial arrangement of reaches across sessions, when compare to LFADS. **d** Hand trajectories linearly decoded from MARBLE embeddings showed much stronger spatial correspondence to ground-truth kinematics than LFADS.

References

- [1] D. M. Mount and S. Arya, “Finding the nearest neighbors for points in d-dimensional euclidean space,” *ACM Transactions on Mathematical Software (TOMS)*, vol. 24, no. 1, pp. 96–103, 1998.
- [2] T. Berry and T. Sauer, “Consistent manifold representation for topological data analysis,” *Foundations of Data Science*, vol. 1, no. 1, pp. 1–38, 2019.
- [3] M. Budninskiy, G. Yin, L. Feng, *et al.*, “Parallel transport unfolding: A connection-based manifold learning approach,” *SIAM Journal on Applied Algebra and Geometry*, vol. 3, no. 2, pp. 266–291, 2019.
- [4] W. Kabsch, “A solution for the best rotation to relate two sets of vectors,” *Acta Crystallographica Section A*, vol. 32, no. 5, pp. 922–923, Sep. 1976.
- [5] V. M. Berline N. Getzler E., *Heat kernels and Dirac operators*, 2nd. Springer, 1996.
- [6] A. Singer and H. T. Wu, “Vector diffusion maps and the connection Laplacian,” *Commun. Pure Appl. Math.*, vol. 65, no. 8, pp. 1067–1144, 2012.
- [7] D. Beaini, S. Passaro, V. Létourneau, *et al.*, “Directional graph networks,” in *International Conference on Machine Learning*, PMLR, 2021, pp. 748–758.
- [8] K. He, X. Zhang, S. Ren, *et al.*, “Deep residual learning for image recognition,” in *2016 IEEE Conference on Computer Vision and Pattern Recognition (CVPR)*, 2016, pp. 770–778.
- [9] W. L. Hamilton, R. Ying, and J. Leskovec, “Inductive representation learning on large graphs,” *Adv. Neural Inf. Process. Syst.*, vol. 2017-Decem, no. Nips, pp. 1025–1035, 2017.
- [10] M. Fey and J. E. Lenssen, “Fast graph representation learning with PyTorch Geometric,” in *ICLR Workshop on Representation Learning on Graphs and Manifolds*, 2019.
- [11] A. Dubreuil, A. Valente, M. Beiran, *et al.*, “The role of population structure in computations through neural dynamics,” *Nat. Neurosci.*, vol. 25, no. 6, pp. 783–794, 2022.
- [12] D. P. Kingma and J. Ba, *Adam: A method for stochastic optimization*, 2014.
- [13] C. Pandarinath, D. J. O’Shea, J. Collins, *et al.*, “Inferring single-trial neural population dynamics using sequential auto-encoders,” *Nat. Methods*, pp. 1–21, 2018.
- [14] M. Denker, A. Yegenoglu, and S. Grün, “Collaborative HPC-enabled workflows on the HBP Collaboratory using the Elephant framework,” in *Neuroinformatics 2018*, 2018, P19.